ACS APPLIED BIO MATERIALS

Article

Nanoceutical Fabric Prevents COVID-19 Spread through Expelled Respiratory Droplets: A Combined Computational, Spectroscopic, and Antimicrobial Study

Aniruddha Adhikari, Uttam Pal, Sayan Bayan, Susmita Mondal, Ria Ghosh, Soumendra Darbar, Tanusri Saha-Dasgupta,* Samit Kumar Ray,* and Samir Kumar Pal*

Cite This: https://doi.org/10.1021/acsabm.1c00238

Read Online

ACCESS | Metrics & More | Article Recommendations | Supporting Information

ABSTRACT: Centers for Disease Control and Prevention (CDC) warns the use of one-way valves or vents in face masks for potential threat of spreading COVID-19 through expelled respiratory droplets. Here, we have developed a nanoceutical cotton fabric duly sensitized with non-toxic zinc oxide nanomaterial for potential use as a membrane filter in the one-way valve for the ease of breathing without the threat of COVID-19 spreading. A detailed computational study revealed that zinc oxide nanoflowers (ZnO NFs) with almost two-dimensional petals trap SARS-CoV-2 spike proteins, responsible to attach to ACE-2 receptors in human lung epithelial cells. The study also confirmed significant denaturation of the spike proteins on the ZnO surface, revealing removal of the virus upon efficient trapping. Following the computational study, we have synthesized ZnO NF on a cotton matrix using a hydrothermal-assisted strategy. Electron-microscopic, steady-state, and picosecond-resolved spectroscopic studies confirm attachment of ZnO NF to the cotton (i.e., cellulose) matrix at the atomic level to develop the nanoceutical fabric. A detailed antimicrobial assay using *Pseudomonas aeruginosa* bacteria (model SARS-CoV-2 mimic) reveals excellent antimicrobial efficiency of the developed nanoceutical fabric. To our understanding, the nanoceutical fabric used in the one-way valve of a face mask would be the choice to assure breathing comfort along with source control of COVID-19 infection. The developed nanosensitized cloth can also be used as an antibacterial/anti CoV-2 washable dress material in general.
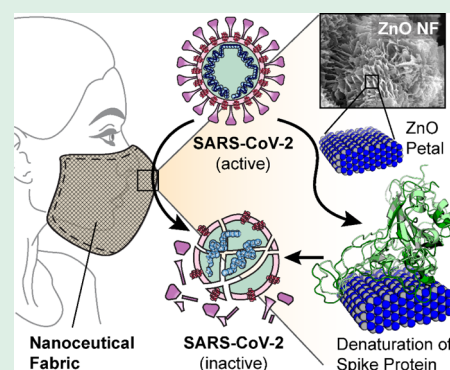
KEYWORDS: COVID-19, nanoceutical, self-cleaning PPE, ZnO nanoflower, antimicrobial fabric, SARS-CoV-2 mimic

INTRODUCTION

The emerging coronavirus disease 2019 (COVID-19) pandemic, caused by severe acute respiratory syndrome-related coronavirus 2 (SARS-CoV-2), has imposed a global socio-economic burden, particularly to the public and private healthcare systems due to unprecedented morbidity, mortality, and economic disruption.[1] At the time of writing, over 81.27 million patients have been infected by SARS-CoV-2, with over 1.77 million deaths worldwide.[2] Recently, some of the vaccine candidates have received conditional approval from various authorities around the world despite suffering from numerous issues like dose, interval between two shots, and so forth. Even after that, it will take several months to reach the common people due to challenges like regulatory issues, large-scale production, and mass distribution to the public.[3] Therefore, the sole line of defence recommended by almost all the apex medical bodies throughout the world is "non-pharmacological interventions" like the use of personal protective equipment (PPE) (e.g., face mask, face shield, gloves, and so forth) and personal hygiene (e.g., handwashing and cough and sneeze etiquette).[4−6] As the world is ready to reopen and most of the

countries are waiting for a second or third wave of virus outbreak, PPE, particularly face masks, has become an integral part of day-to-day life. Although face masks are commonly used to provide protection to the wearer (e.g., first responders), they were originally introduced to protect surrounding persons.[7] Generally, the term "face mask" covers a broad range of PPE that reduces the transmission of respiratory particles or droplets.[7]

Recently, Centers for Disease Control and Prevention (CDC) warned against the use of one-way valves or vents in face masks for potential threat of spreading COVID-19 through expelled respiratory droplets.[8] However, the face masks without valves or vents can cause several health problems and severe discomfort to the wearer.[9,10] Some pieces

of evidence suggest that commonly available N95 face masks can lead to changes in blood oxygen (O_2) and carbon dioxide (CO_2) levels when used for long periods, especially by people who are elderly or obese or have chronic obstructive pulmonary disease.[9−11] Other adverse health effects range from increased blood pressures, increased heart rates, chest pain, and hypercapnia.[12,13] One of the feasible solutions to this problem is by covering the valve or vent with a porous filter that can either trap or kill the microorganisms including viruses, alongside allowing the air to flow across. Unfortunately, no study has been performed up to date to design such filters or to address the problem by other means. In this regard, filters made up of natural fabrics (e.g., cotton) functionalized with antimicrobial agents could be an effective solution.

Although a vast diversity of organic compounds with recognized antimicrobial activity have been incorporated into polymers in order to develop antimicrobial fibers, they exhibit several drawbacks related to their thermal and chemical instability, which could lead to difficulties throughout the functionalization process and also produce fibrous mats with limited antimicrobial activity due to partial decomposition of the antimicrobial agent.[14] Moreover, the massive use of antibiotics has led to another global problem, the origination of antibiotic-resistant bacteria.[15,16] Thus, there is a growing need to explore novel antimicrobial agents to functionalize the natural or synthetic fabrics not only to prevent COVID-19 spread but also for other applications like clothing materials for patients to stop hospital-acquired infections, which is also a global challenge.

Consequently, nanoscale materials with unique and tuneable physicochemical properties (i.e., higher chemical, mechanical, and thermal stability) are interesting elements for preparation of hygienic surfaces. For example, silver ions and silver-based nanocompounds are highly toxic to microorganisms, showing strong biocidal effects on various species of bacteria.[17−19] Gold nanoparticles,[20,21] bimetallic nanomaterials (e.g., Ag/Au, Ag/Pt, and so forth),[22,23] graphene-based materials,[24] and metal oxide nanoparticles [e.g., titanium dioxide (TiO_2), copper oxide (CuO), silica (SiO_2), and so forth][25−27] are other examples. However, they all suffer from the problem of inherent toxicity of the nanomaterials, limiting their human use.[28−32] Recently, several ultrasmall metal nanoclusters particularly of gold (Au) and silver (Ag) have shown wide-spectrum antimicrobial activity.[33−36] Even these ultrasmall metal nanoclusters have been impregnated into biocompatible hydrogels to eradicate bacterial biofilms.[34] The nanoclusters induce metabolic imbalance in the microorganism, leading to enhanced reactive oxygen species generation, which in turn kills the microbe.[33] One of the advantages of these nanoclusters is the possibility of atomic-level control of the size, structure, composition, and surface functionalization leading to a more personalized treatment strategy.[37] Moreover, they do not pose the problem of antibiotic resistance. However, biocompatibility and cytotoxicity of these materials remain a key concern. Therefore, it is of considerable interest to design a nanoparticle-functionalized fabric (i.e., nanoceutical fabric) that can efficiently kill or trap microorganisms without any harmful side effect to the user.

In this study, we have rationally designed a nanoceutical cotton fabric duly sensitized with the non-toxic zinc oxide (ZnO) nanomaterial for potential use as a membrane filter in the one-way valve or vent of the face mask for the ease of breathing without the risk of COVID-19 spread. A comprehensive computer-assisted simulation study revealed the unique potential of ZnO nanoflowers (ZnO NFs) having nearly two-dimensional nanopetals in entrapment and denaturation of coronavirus spike protein (resulting into eradication of the virus), which mediates the viral pathogenesis through attachment to angiotensin converting enzyme-2 (ACE-2) receptors in the human respiratory tract. Subsequently, we have synthesized ZnO NF on a natural cotton fiber matrix using a one-pot hydrothermal-assisted approach. In-depth electron-microscopic, steady-state, and picosecond-resolved spectroscopic studies confirm the attachment of ZnO NF to the cellulose matrix of cotton at the atomic level to develop the nanoceutical fabric filter. An exhaustive antimicrobial study using a capsule containing virulent *Pseudomonas aeruginosa* as a mimic of coronavirus (as the lectins in *P. aeruginosa* share similar homology to coronavirus spike protein) reveals excellent antimicrobial (bactericidal) efficiency of the developed nanoceutical fabric filter. To our understanding, the novel nanoceutical fabric used in the one-way valve of a face mask would be the choice to assure breathing comfort along with source control of COVID-19 infection. The developed nanosensitized cloth can further be used as an antibacterial (as well as anti SARS CoV-2) dress material in general to stop hospital-acquired infections.

■ RESULTS AND DISCUSSION

Prediction of the Potential Antiviral Nanostructure and Model Experimental Organism. SARS-CoV-2 (Figure 1a,b), generally initiates its infection process by binding to functional receptors on the membrane of a host cell.[38] In the case of humans, membrane-bound ACE-2 (the functional host receptor) plays a crucial role in pathogenesis of COVID-19 providing viral entry to human cells (Figure 1c,d).[39,40] The spike (S) protein present in the outer surface of SARS-CoV-2 binds to human ACE-2 with a very strong affinity and subsequently mediates membrane fusion leading to host cell entry of the virus (Figure 1c,d).[39,41,42] The computed binding energy for human ACE-2 and SARS-CoV-2 S-protein from the crystal structure (PDB ID: 6LZG; Figure 1d) of the complex was found to be −20.28 kcal mol^{-1}. Following minimization of the complex under the optimized potentials for liquid simulations[43] (OPLS) force field, the binding energy drops to −29.83 kcal mol^{-1}. This strong binding energy can be attributed to the large surface area at the protein−protein interface and several favorable intermolecular interactions including hydrogen bonding, ionic, and hydrophobic interactions. Hence, it is difficult to develop small-molecule competitive inhibitors that can disrupt such an elaborate molecular recognition. Therefore, we looked into the prospective nanomaterials having a similar magnitude to ACE-2 protein along with the ability to compete for the viral S-protein binding. In this regard, our primary choice was ZnO considering its biocompatibility and known antimicrobial and antiviral effect.[44−46] In a computer simulation, a spherical ZnO nanoparticle (∼30 nm diameter, similar dimensions of ACE-2) was constructed and its interaction with the viral S-protein was studied (Figure 1e). The spherical nanoparticle provided a convex surface for interactions similar to the ACE-2 receptor protein. Since the geometry of the nanosurface at the binding region is known to affect the protein−nanomaterial interaction,[47,48] we further simulated the interaction of S-protein with the flat sheet-like ZnO surface having various exposed
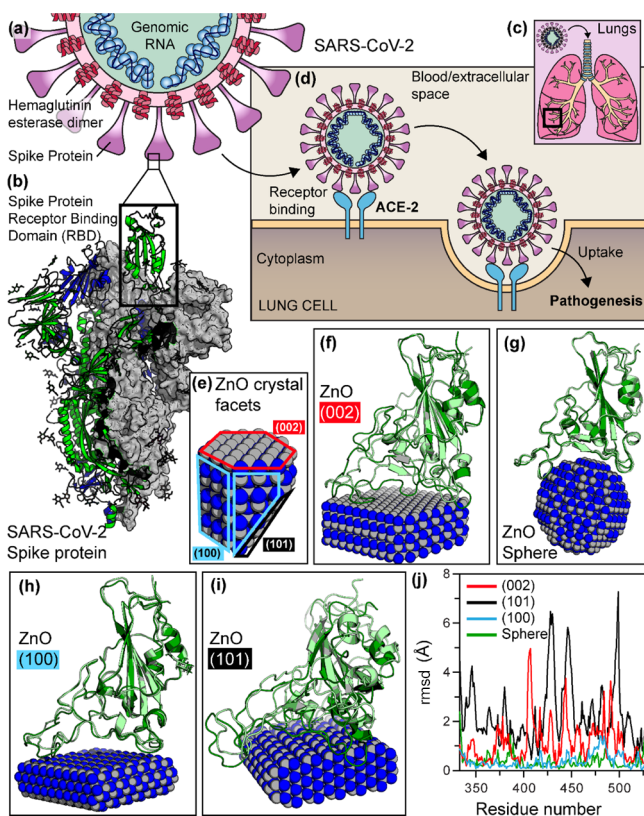
Figure 1. Interaction of SARS-CoV-2 spike protein RBD with ZnO nanofacets leads to denaturation of spike RBD. (a) Schematic representation of the SARS-CoV-2 structure. This is an enveloped, positive sense RNA virus having spike proteins at the outer surface. (b) Side view of the pre-fusion structure of the SARS-CoV-2 spike protein with a single RBD in the upconformation. (c) SARS-CoV-2 infection through the human respiratory tract. (d) Internalization of SARS-CoV-2 by membrane fusion. The spike protein binds to ACE-2 of the host cell via RBD and further releases its RNA to exert pathogenesis. (e) Crystal facets of the wurtzite zinc oxide (ZnO) nanostructure used in computational studies. (f−i) Binding of spike RBD (molecular docking) with different facets of the ZnO nanostructure as well as the spherical ZnO nanoparticle. The spike protein strongly binds to the ZnO crystal facets and denatures upon interaction. The native structure of the protein is represented by the light color, while the dark color represents the denatured structure after interaction. (j) rmsd values of each amino acid after energy minimization under OPLS show the degree of denaturation.

crystal facets (⟨100⟩, ⟨101⟩, and ⟨002⟩) as observed in the X-ray diffraction (XRD) pattern (*vide infra*).

As evident from the molecular docking study, the SARS-CoV-2 S-protein can bind favorably with both the ZnO nanosphere and the flat facets (⟨100⟩, ⟨101⟩, and ⟨002⟩) of the ZnO nanostructure with binding energies of −17, −11, −21, and −16 kcal mol^{-1}, respectively. Binding on the ⟨101⟩ ZnO nanosurface was very much comparable with that of ACE-2. After the energy minimization of the docked complexes, the binding energies were found to be −21, −13, −40, and −22 kcal mol^{-1}, respectively. Figure 1e−i shows the bound conformations of spike protein with the ZnO nanosphere and various facets on ZnO nanosurfaces. Interestingly, when structural deviations (in terms of root-mean-square deviation, rmsd) were studied and compared between the docked and energy-minimized conformations of the spike receptor binding domain (RBD) (Figure 1j), large structural perturbations

become evident in the binding regions of SARS-CoV-2 S-protein due to binding on ZnO nanofacets. Least change was observed in the case of the nanosphere, whereas most change occurred on the ⟨101⟩ facet of ZnO. Since the structure and function of proteins are highly correlated, infliction of a large structural perturbation in the protein structure by an inhibitor or ligand is generally associated with its loss of function.[43] The observed *in silico* structural changes, therefore, indicate that the viral S-protein may lose its pathological function if it comes in contact with the ZnO nanosurface.

Bearing in mind the transmissibility and pathogenicity of SARS-CoV-2 as well as unavailability of the SARS-CoV-2 strain and biosafety requirements for experimental studies, we looked for similar organisms as an alternative model preferably of the bacterial origin having adhesion proteins analogous to viral S-protein. Lectin-A (LecA) protein of *P. aeruginosa* (Figure 2a) was found to show a high degree of similarity in the binding site residues as evident from the amino acid sequence alignment depicted in Figure 2a,b. In the largest 32 amino acid overlap region (14−45:149−180), the two proteins showed 28.1% identity and 62.5% similarity with a Waterman−Eggert score of 52. Detailed sequence alignments of the Spike RBD and LecA protein are given in the Supporting Information. Apart from the structural similarity, LecA resembles the function of viral S-protein and mediates bacterium-host cell recognition and adhesion, which are the critical steps in initiating *P. aeruginosa* pathogenesis.[49] Interestingly, for both SARS-CoV-2 and *P. aeruginosa*, lungs are the primary target organs, and both of them cause similar acute and chronic lung infection.[49−51] Therefore, considering the structural and functional resemblances in a possible example of molecular mimicry, *P. aeruginosa* LecA was chosen as an alternative to SARS-CoV-2 S-protein for subsequent computational and experimental binding studies with the ZnO nanostructures.

The molecular docking study illustrates that the *P. aeruginosa* LecA protein can bind favorably with the ZnO ⟨100⟩, ⟨101⟩, and ⟨002⟩ nanofacets as well as on the ZnO nanosphere with comparable binding energies of −9, −11, −12, and −11 kcal mol^{-1}, respectively. After the energy minimization of the docked complexes, the binding energies were found to be −11, −14, −26, and −17 kcal mol^{-1}, respectively. Figure 2c−f shows the bound conformations of LecA protein with the ZnO nanosphere and nanofacets, respectively. Structural deviations in terms of rmsds were studied and compared between the docked and minimized complexes and graphically represented in Figure 2g. It is evident from Figure 2g that large structural perturbation, similar to the viral S-protein, takes place in the binding regions of LecA protein on the ZnO nanofacets.

Thus, the computational binding study shows that the ZnO nanosurface can trap the adhesion proteins of SARS-Cov-2 as well as that of *P. aeruginosa*. The sheet-like flat ZnO nanostructures not only bind these adhesion proteins (i.e., viral S-protein and LecA) but also impart large-scale structural perturbation in the bound protein (i.e., denaturation), leading to functional impairment and disinfectant effects. Therefore, based on the computational findings, *P. aeruginosa* (having LecA) was chosen as a model SARS-CoV-2 mimic, and the ZnO sheet-like nanostructure was selected as an antimicrobial agent for subsequent experimental validation.

Design of the Natural Cotton Fabric Functionalized with ZnO NF Featuring Flat Sheet-like Petals. Encour-
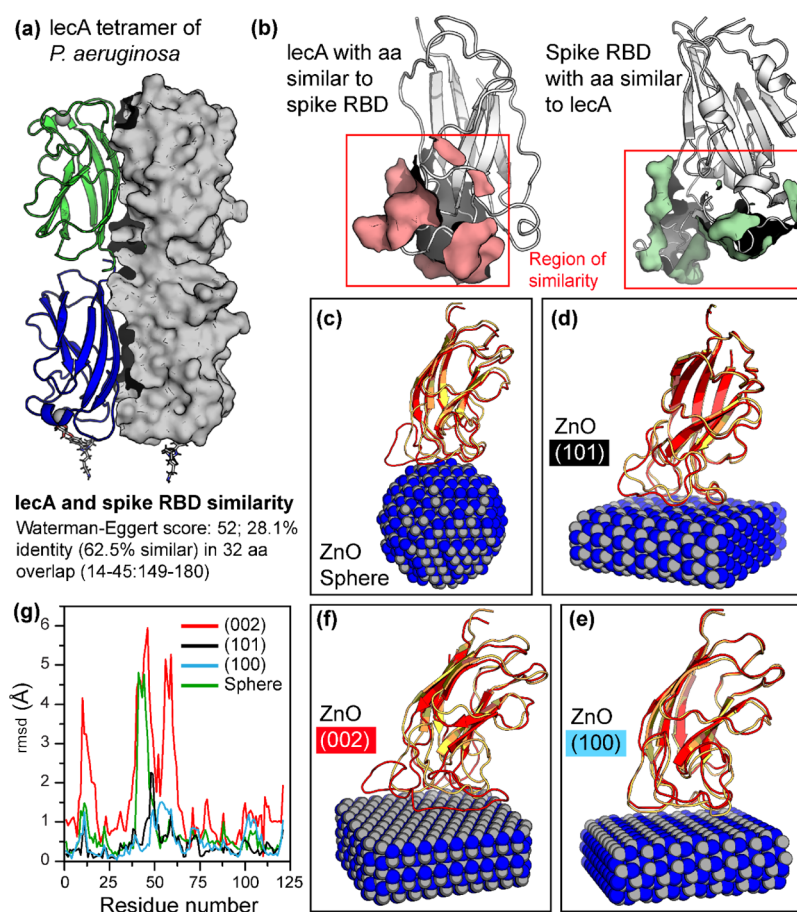
Figure 2. Interaction of a mimic of SARS-CoV-2 spike RBD, lecA of *P. aeruginosa*, with ZnO nanofacets leads to denaturation. (a) Tetrameric crystal structure of *P. aeruginosa* lecA. (b) Computed structural similarity between lecA and spike RBD. (c−f) Binding of lecA (molecular docking) with spherical ZnO nanoparticles as well as different facets of the ZnO nanostructure. LecA strongly binds to the ZnO crystal facets and denatures upon interaction. The native structure of the protein is represented by the light color, while the dark color represents the denatured structure after interaction. (g) rmsd values of each amino acid after energy minimization under OPLS show the degree of denaturation.
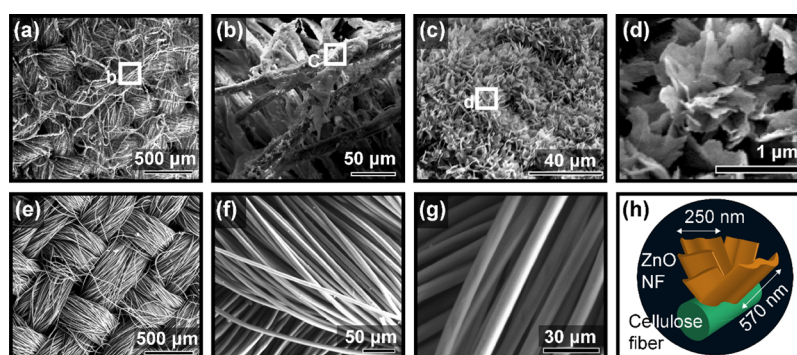
Figure 3. of the developed ZnO NF-decorated cotton cloth at different magnifications. (a−c) Low-magnification scanning electron micrograph of the ZnO NF-decorated cotton cloth. (d) High-magnification SEM shows the self-assembled petal-like structures of a single NF. (e−g) Scanning electron micrograph of the bare cotton cloth showing the constituent cellulose fibers. (h) Schematic representation of ZnO NF as observed under SEM.

aged by the *in silico* studies, we intended to decorate the natural cotton fabric with flat ZnO sheet-like structures, which eventually self-assembled into more complex rose-like ZnO NF during the hydrothermal-assisted low-temperature one-pot synthesis process (detailed in the "Materials and Methods" section). The scanning electron micrographs confirm the formation of the flower-like morphology of ZnO on the surface of the cotton fiber (Figure 3a−d). Figure 3e−g shows the

scanning electron micrographs of the bare cloth. The flat sheet-like petals of the flower have a length of ∼600−850 nm and a diameter of ∼150−300 nm with an aspect ratio of ∼3 (schematically represented in Figure 3h). It should be noted that the surface of the petals is not smooth, rather coated with small granules of nanoparticles. Energy-dispersive X-ray analysis confirms the presence of ZnO in the nanostructure (Figure S1). Elemental mapping confirmed the uniform
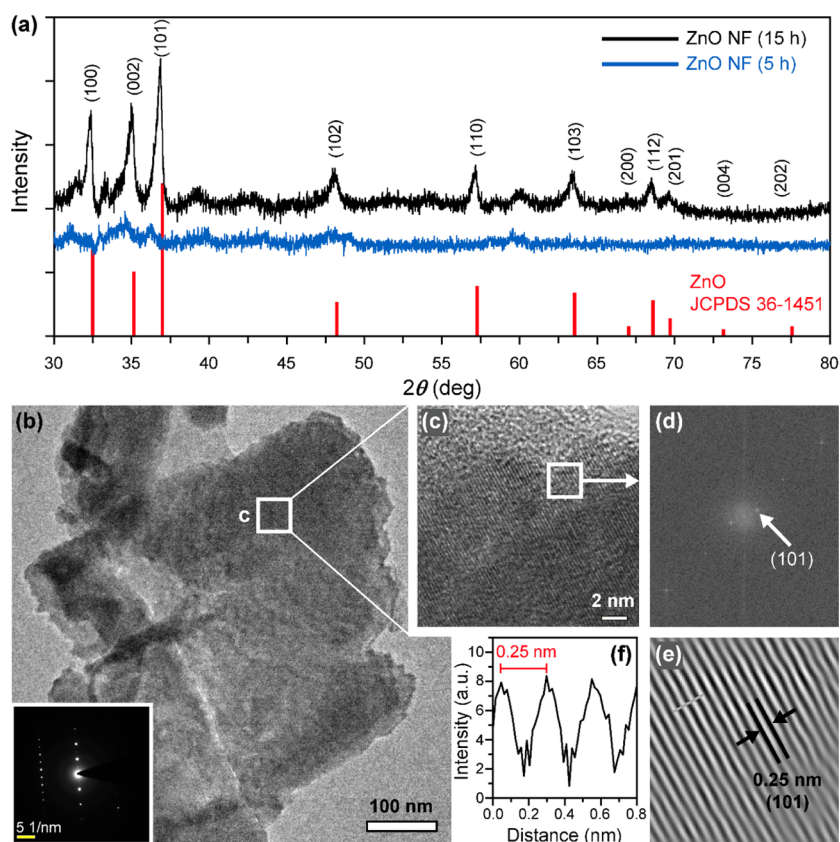
Figure 4. Characterization of the ZnO NF-decorated cotton cloth. (a) XRD pattern of the ZnO NF-decorated cotton cloth at different synthesis phases. (b) Transmission electron micrograph of a single fully grown petal. The inset shows an SAED pattern of the ZnO petal. (c) HRTEM image of a part of the petal indicated as a white box in (b). (d) Corresponding FFT image. The (101) plane is indicated. (e) Reconstructed lattice image from FFT. (f) Interplanar spacing plot shows a *d*-spacing of ∼0.25 nm.

distribution of ZnO NF on the surface of the cotton matrix (Figure S2). Thermal gravimetric (TG)−differential thermal analysis shows ∼9% (w/w) loading of ZnO NF to cellulose fibers (Figure S3).
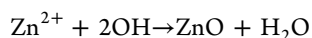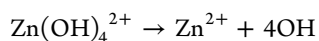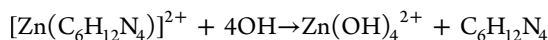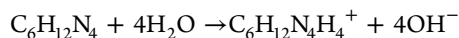
At the outset, we investigated the growth of the ZnO phase on the cotton clothes using the XRD technique. With 5 h of intermediate growth time, the ZnO phase is not distinguishable properly as the prominent XRD peaks are suppressed by the broad hump of cellulose within the Bragg angle (2θ) range between 31 and 38° in Figure 4a. Nevertheless, the signature of the ⟨101⟩ plane of ZnO at ∼36.2° can be traced from the XRD pattern. The growth of ZnO becomes quite dominant when the growth time is increased to 15 h. In this case, the diffraction peaks appearing at 2θ of 31.8, 34.4, 36.1, 47.4, 56.6, 63.0, 68.0, and 69.2° represent the ⟨100⟩, ⟨002⟩, ⟨101⟩, ⟨102⟩, ⟨110⟩, ⟨103⟩, ⟨112⟩, and ⟨201⟩ planes of ZnO nanocrystals, respectively. The observed peaks are in good agreement with those for hexagonal closed-packed ZnO having the wurtzite structure [lattice constants *a* = 3.249, *c* = 5.206 Å; space group *P6₃mc* (186)] as reported earlier (JCPDS 36-1451).[52] Sharp diffraction peaks indicate good crystalline quality of the synthesized NFs, and the absence of any additional peak directs toward the high purity of the material. The highly intensified peak at 36.1° indicates the dominance of the ⟨101⟩ plane in the material.

The transmission electron microscopy (TEM) image (Figure 4b) shows the size of a single ZnO NF petal to be ∼600 × 300 nm. The high-resolution TEM (HRTEM) image taken at the center of the petal indicates the presence of the
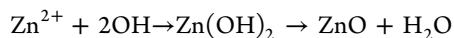
⟨101⟩ plane (Figure 4c). The presence of distinct bright spots in the selected area electron diffraction (SAED) pattern (Figure 4d) corresponds to the crystalline nature of the petals. Fast Fourier transformation (FFT) shows that the crystallite is dominated by the ⟨101⟩ plane of ZnO, with a lattice fringe spacing of 0.25 nm (Figure 4e,f). Further, as shown in Figure 5a, the formation of the nanorod-like morphology can be observed when the reaction time is reduced (i.e., 5 h). The surface of the nanorods appears to be rough and can be originated from the presence of a large number of crystallites. The SAED pattern shows small spots within the diffused ring and reveals the polycrystallinity of the nanorods as each spot arises from the Bragg reflection from individual crystallites (Figure 5a inset). The rings can be indexed as ⟨101⟩, ⟨102⟩, and ⟨200⟩ of the wurtzite phase of ZnO, which exactly correlates with the XRD pattern (Figure 4a). Next, a close look of the nanorod at different locations (marked as c,d in Figure 5b) reveals the presence of the ⟨101⟩ and ⟨002⟩ planes of ZnO with interplanar spacings of ∼0.25 and 0.26 nm, respectively (Figure 5c−g). The exhibition of polycrystalline nature of the nanorods with various crystallites is different from nanorods grown on crystalline surfaces (e.g., Si). Thus, it can be anticipated that the use of the cotton substrate in the synthesis process plays a big role in forming nanorods with exposed crystallites on the surface (Figure 5). In fact, the functional groups present in the cellulose fibers act as nucleation sites for the growth of nanorods (step 1 in Figure 6). It can be noted that in HMT-based hydrothermal synthesis, Zn(OH)₂ acts as the nucleation agent according to the following equations:[53]
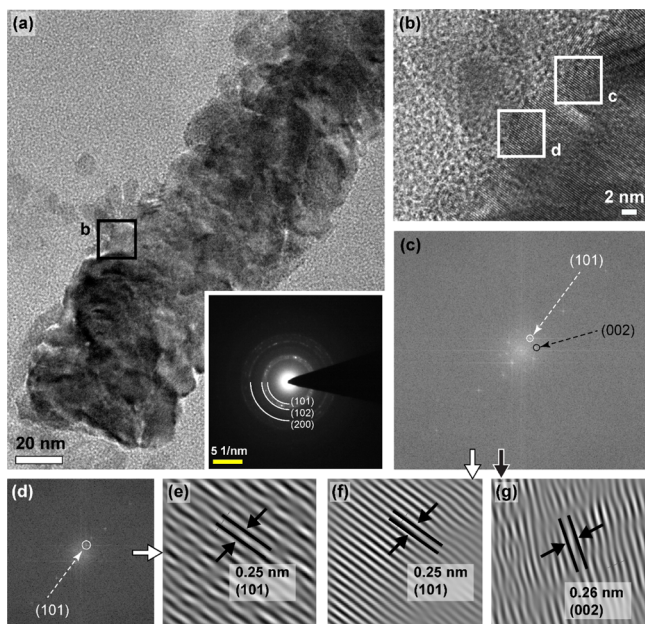
Figure 5. TEM image of the ZnO NF petal at an intermediate growth time (5 h). (a) TEM of a single growing petal. The inset shows the SAED pattern of the growing petal. (b) HRTEM of the petal. (c,d) Corresponding FFT image from different areas indicated as a white box in (b). The (101) and (002) planes are indicated. (e−g) Reconstructed lattice image from FFT shows the fringe pattern and d-spacing.

$$C_6H_{12}N_4 + 4H_2O \rightarrow C_6H_{12}N_4H_4^+ + 4OH^-$$

$$[Zn(C_6H_{12}N_4)]^{2+} + 4OH \rightarrow Zn(OH)_4^{2+} + C_6H_{12}N_4$$

$$Zn(OH)_4^{2+} \rightarrow Zn^{2+} + 4OH$$

$$Zn^{2+} + 2OH \rightarrow ZnO + H_2O$$

or

$$Zn^{2+} + 2OH \rightarrow Zn(OH)_2 \rightarrow ZnO + H_2O$$

In the present investigation, the abundant and random distribution of these functional groups based nucleation sites on the cellulose fiber surface provides a continuous platform for ZnO growth along the direction of fibers (step 1 in Figure 6). As the nucleation and the subsequent growth process occur on the outer circumference of the cellulose fibers, the fiber plays the role of a template to form a nanorod-like one-dimensional structure (step 2 in Figure 6). Now, the random distribution of the functional groups leads to the randomly oriented nucleation sites, and consequently, the growth is evident to be different in different directions. The observation of the rough surface with different crystallites of the ⟨101⟩ and ⟨002⟩ planes is the consequence of such a growth process.

It is worth mentioning here that the method used to functionalize the cotton fibers is widely applicable to other substrates. Similar strategies were used to functionalize glass and nylon fishing nets previously.[54,55] However, in both the cases, distinct nanorods were formed instead of NF, which may be due to the more oriented distribution of the surface functional groups. Also, from our understanding, the size of the cotton fibers will not impact the fabrication results. However, the type of functional groups may have an impact on the fabrication process, which needs to be explored in future with greater detail.

Now, it is well established that in ZnO crystals, the surface energy (per mole) varies with the direction as $\gamma_{[0001]} < \gamma_{[11-20]} < \gamma_{[10-10]}$.[56] Hence, the growth of the ⟨002⟩ plane along the [0001] direction is highly favorable from a thermodynamic point of view. Thus, the nanorods with exposed ⟨002⟩ planes offer chances for further growth. As a result, with increased reaction time, the nanorods suffer two-dimensional growth, that is, along horizontal as well as vertical directions to the surface of the fiber, leading to the development of petal-like features (step 4 in Figure 6). To ensure this fact, TEM analysis has been performed on four different edges of the fully grown petal. In none of these areas, any signature of the ⟨002⟩ plane has been found. It is well known that a plane with a higher growth rate disappears quickly.[57] Thus, the disappearance of the ⟨002⟩ plane confirms the speculated lateral growth of the nanorods to form the petals. Subsequent self-assembly of such petal-like features leads to the formation of a flower-like morphology of ZnO at a higher reaction time (step 5 in Figure 6).

Figure 7a shows the absorbance spectrum recorded from bare cotton cloths and ZnO NF decorated cotton cloths. As the constituent of the cotton fiber is cellulose, the observed absorption bands at 200−220 and 270−290 nm could be assigned to oxidized xylans and monocarboxyl celluloses due to the presence of carboxyl and carbonyl groups, respectively.[58] Furthermore, the absorption bands at 230−250 and 290−320 nm could be assigned to heteroaromatics of the furan and pyron types, respectively, and the low-intensity absorption shoulder above 300 nm to conjugated heteroaromatics.[58] Functionalization with ZnO NF leads to the appearance of the characteristic ZnO absorption edge at 365 nm which is blue-shifted by 8 nm relative to the bulk exciton absorption (373 nm).[59] Correspondingly, ZnO NF exhibited a slightly higher optical energy gap (E_g) of 3.44 eV with respect to bulk ZnO (3.37 eV) (Figure 7a inset). The slight change in the absorption edge and E_g can be well explained by the oriented attachment of multiple ZnO nanorods in the flower-like morphology.[59,60]

The fluorescence emission spectra of the cotton cloth in the solid state (Figure 7b) show an intense peak around 430 nm and a broad shoulder ranging from 470 to 560 nm when excited at 375 nm. The observed emission pattern of the cotton cloth exactly matches to the previously reported photoluminescence characteristics of cellulose fibers.[58,61] Gavrilov and Ermolenko (1966),[62] who studied photoluminescence of cellulose in great detail, have suggested that the broad emission band of cellulose originates from three different types of excitation centers. The presence of multiple excitation maxima (i.e., 265, 350, and 390 nm) in the excitation spectra of the bare cotton cloth (Figure 7b inset) further supports their findings. Functionalization with ZnO NF significantly quenched the emission of the cellulose constituent (Figure 7b), which indicates possible interactions between ZnO NF and cellulose fibers. The observed increase in the λ_{em} 410 nm/λ_{em} 450 nm ratio could be due to a possible interaction between the Zn-vacancy state of ZnO NF and the OH groups of cellulose fibers (O=C−O−Zn) as previous studies suggest that the presence of carboxylic groups in the anhydroglucose units shifts the emission maxima of cellulose to shorter wavelengths (blue shift).[58,61,63] A detailed computational study (i.e., molecular docking) further supports the
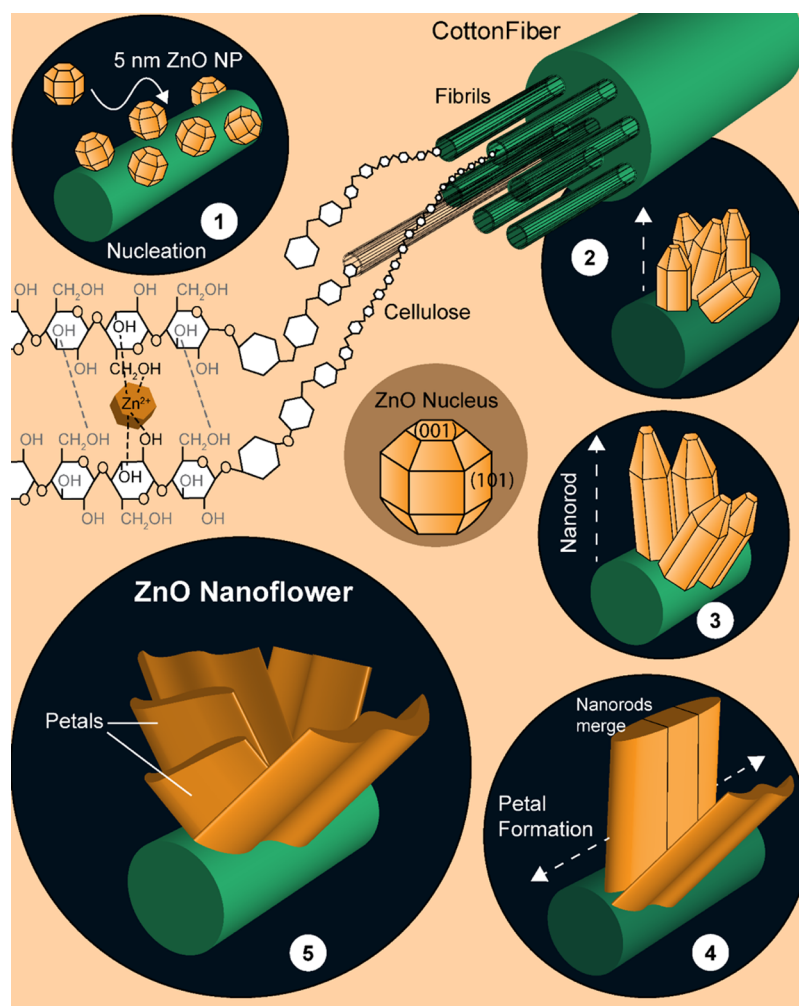
Figure 6. Schematic representation of the different phases of ZnO nanoflower growth on the cotton cloth constituted with cellulose fibers. The numbers (1−5) indicate different steps of the growth. See the text for details.

strong binding of ZnO NF with the cellulose fiber, mostly through hydrogen bonding. The calculated binding energies per unit area of the cellulose fiber with different facets of the ZnO nanostructure were found to be −21 kcal mol^{-1} nm^{-2} (sphere), −43 kcal mol^{-1} nm^{-2} [⟨002⟩ facet], −41 kcal mol^{-1} nm^{-2} [⟨100⟩ and ⟨110⟩ facets], and −39 kcal mol^{-1} nm^{-2} [⟨101⟩ facet] (Figure S4). The highly negative binding energies indicate stronger attachment between the cellulose fiber and ZnO NF.

To get further insight into the quenching mechanism, we studied the excited-state fluorescence lifetime of cellulose (i.e., cotton cloth) and ZnO NF-decorated cellulose. Interestingly, the fluorescence lifetime of both the samples remained unchanged at 450 nm (λ_{ex} 375 nm) (Figure 7c), while a decrease was observed at 550 nm (λ_{ex} 375 nm) upon ZnO NF decoration (Figure 7d). This could well be interpreted by the existence of several luminescent centers (originating from the presence of conjugated chromophores of various origins) in the cellulose.[62] One possible mechanism behind the observed decrease in the fluorescence lifetime of ZnO NF-decorated cellulose could be due to the photoinduced electron transfer from the lowest unoccupied molecular orbital level of the low-energy excitation centers (near the red end) of cellulose to the conduction band of ZnO, resulting in the luminescence quenching of cellulose.[64] The presence of a very fast

component (i.e., 25 ps) in the excited-state lifetime decay of ZnO NF-decorated cellulose further supports our conjecture. In contrast, due to the mismatch in the energy levels, the high-energy excitation centers (near the blue end) of cellulose cannot undergo such electron or energy transfers. The quenching in this region is static in nature and may be originated due to ground-state interactions between ZnO NF and cellulose which we explained in the earlier section. In summary, the results of our optical studies confirm the attachment of ZnO NF to the cellulose fibers of the cotton cloth.

Antimicrobial Activity of the ZnO NF-Functionalized Cotton Fabric. The antimicrobial activity of the ZnO NF-decorated cotton fabric was evaluated against the SARS-CoV-2 mimic pathogenic capsule containing (having LecA, the mimic of viral spike protein; *vide* computational studies in the earlier section) Gram-negative model bacteria *P. aeruginosa*. To directly assess the antimicrobial effect, after 1 h of incubation (in the dark, 37 °C) over the ZnO NF-decorated cotton cloth and bare cotton cloth, *P. aeruginosa* was transferred and cultured on a Luria−Bertani (LB) agar medium (i.e., the plate count assay) for 12 h (at 37 °C). The original bacterial inoculum, which was employed over the fabrics for initial incubation, served as a control. As shown in the photographs of the agar plates after 12 h (Figure 8a), a clear killing activity
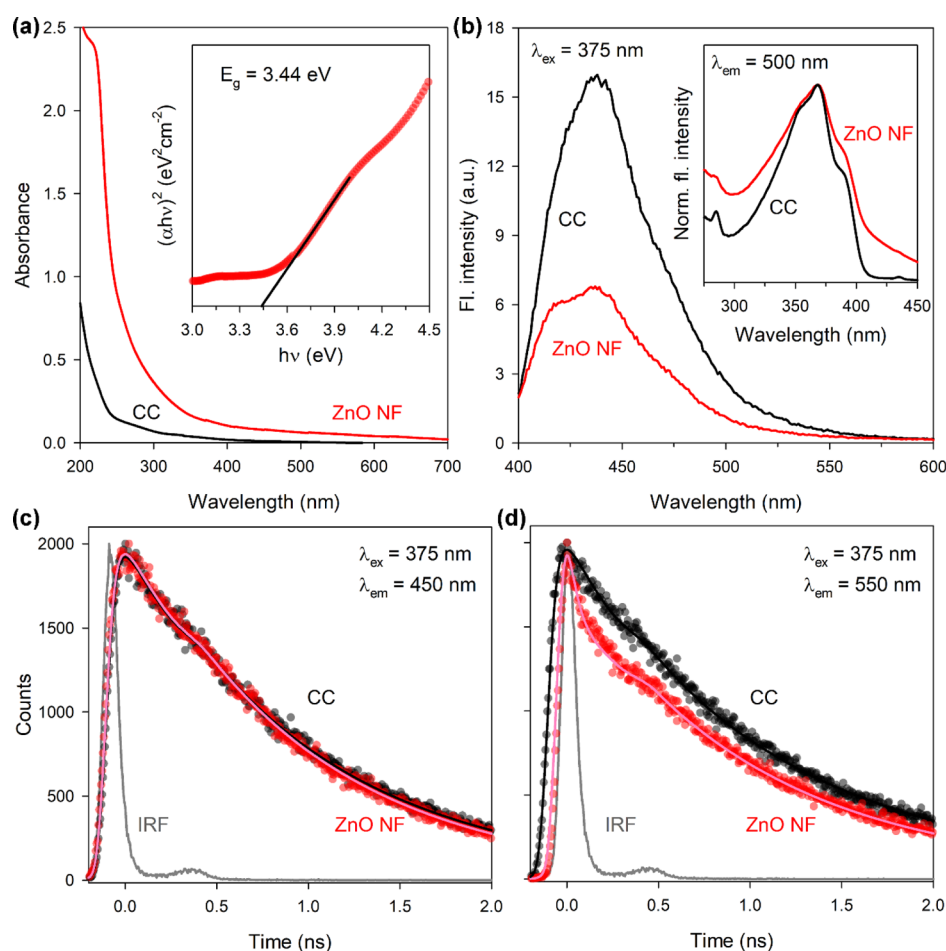
Figure 7. Spectroscopic characterization of the ZnO NF-decorated cotton cloth. (a) UV–vis absorbance spectra of the ZnO NF-decorated cotton cloth and the bare cotton cloth. The inset shows Tauc's plots for determination of the band gap energy. (b) Steady-state fluorescence emission spectra show quenching of cotton cloth fluorescence (originating from the constituent cellulose) upon ZnO NF decoration. The inset shows the corresponding change in fluorescence excitation spectra. (c,d) Picosecond-resolved transients show quenching of fluorescence lifetime of the constituent cellulose by ZnO NF at longer wavelengths.

was observed in the case of the ZnO NF-functionalized cotton fabric resulting into very few colonies. Colony count shows (Figure 8b) that in the ZnO NF-functionalized cotton fabric, the bacterial growth was ~79% lower compared to the control $[P < 0.0001; F(2,15) = 303.2$, one-way analysis of variance (ANOVA)$]$ and ~54% lower compared to the bare cotton fabric $[P < 0.0001; F(2,15) = 303.2$, one-way ANOVA$]$.

Further, the antibacterial effect of the ZnO NF-decorated cotton cloth on the *P. aeruginosa* growth kinetics was evaluated in liquid LB media. The bacterial growth was monitored by the measurement of the optical density at 600 nm (OD_{600}) as a reflection of the bacterial concentration in the culture. After 1 h of incubation over the respective fabrics (inoculation at 1×10^6 CFU/mL), we started monitoring the growth kinetics. The original bacterial inoculum, which was employed over the fabrics for initial incubation, served as a control. Figure 8c clearly indicates that the ZnO NF-decorated cotton cloth caused complete inhibition of growth and this was even continued for 14 h. The bare cotton cloth also showed a weaker growth inhibition. The growth rate was ~10 times lower in the case of the ZnO NF-functionalized cotton fabric compared to both the control $[P < 0.0001; F(2,15) = 1062,$ one-way ANOVA$]$ and bare cotton fabric $[P < 0.0001; F(2,15) = 1062,$ one-way ANOVA$]$ (Figure 8c inset).

Our computational studies have suggested that ZnO NF can simultaneously bind and denature *P. aeruginosa* LecA (SARS-CoV-2 spike protein mimic), resulting into disruption of the bacterial cell membrane, which eventually is responsible for the observed antimicrobial activity. In order to confirm that ZnO NF disrupts the bacterial membrane, *P. aeruginosa* cells were treated with PI after incubation with the ZnO NF-decorated cotton fabric. It is worth mentioning here that PI is a small-molecule dye that upon binding to double-stranded DNA fluoresces red upon excitation, and it cannot cross an intact cytoplasmic membrane.[65,66] We expected that ZnO NF-induced membrane disruption would lead to an increase in nucleic acid staining by PI compared to that of the control or bare cotton cloth-treated ones. As shown in Figure 8d,e, control bacteria as well as bacteria incubated with the bare cotton fabric remained unstained to PI. In comparison, intracellular PI staining was clearly visible in cultures exposed to the ZnO NF-decorated cotton fabric (Figure 8f). We further evaluated the number of viable cells using differential staining with DAPI and PI. As discussed earlier, PI generally stains the membrane-disrupted cells, whereas DAPI stains all nuclear materials irrespective of their viability. The differentially stained images of control and cotton fabric-inoculated bacteria show more number of viable cells than dead cells (ratio ~ 1.2)
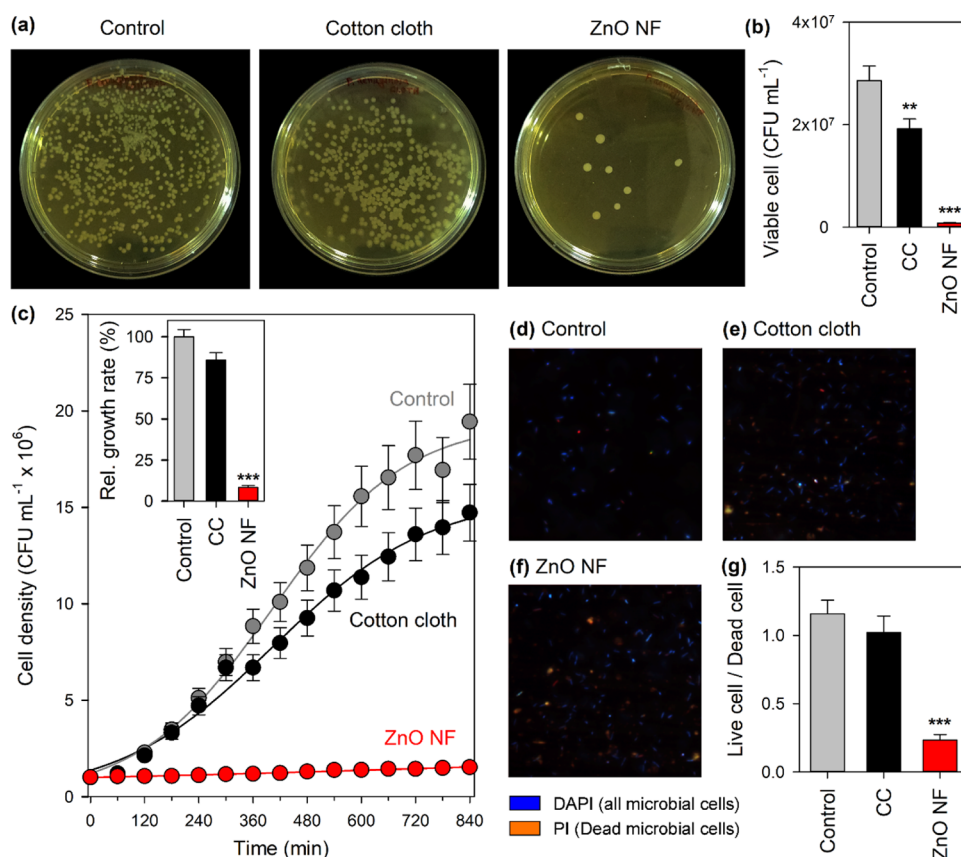
Figure 8. Antimicrobial activity of the ZnO NF-decorated cotton fabric on *P. aeruginosa*, a mimic of SARS-CoV-2. (a) Digital photographs of *P. aeruginosa* colonies on the agar plate after treatment with the ZnO NF-decorated cotton cloth and the bare cotton cloth. (b) Bacterial cell count after 12 h of incubation. (c) Growth pattern of *P. aeruginosa* treated with the ZnO NF-decorated and bare cotton cloths. The inset shows relative growth rates. (d–f) Micrographs of bacteria after DAPI-PI differential staining. (g) Corresponding ratio of live vs dead cells.

(Figure 8g). In contrast, the number of living cells was significantly reduced in the case of the ZnO NF-functionalized cotton fabric (~0.45) (Figure 8g).

Next, we investigated the antimicrobial ability of the ZnO NF-decorated cotton fabric toward Gram-positive bacteria *Staphylococcus aureus*. The results of the plate count assay showed the antimicrobial activity to be significant but lower compared to *P. aeruginosa* (Figure S5), which may be due to the absence of the S-protein mimic in *S. aureus*.

In one of the recent studies, it was observed that the nanoparticles having an anionic surface showed lower antialgal and antiyeast activity compared to those having a cationic surface.[67] The probable explanation could be the poor adhesion of anionic particles to the microbial cell membranes (anionic in nature) due to electrostatic repulsion.[67] However, the particle–cell membrane electrostatic adhesion in the case of cationic nanoparticles leads to enhanced antiyeast and antialgal action.[67] As hydrothermally produced ZnO has a positive surface charge and *P. aeruginosa* has a negative surface charge, there is a possibility that the bacteria bind to NF predominantly through electrostatic interactions between bacterial glycolipids and NF. Therefore, in order to understand the role of charge–charge interactions in the antimicrobial activity, we have decorated the cellulose fiber of the cloth with positively charged poly-L-lysine and repeated the antimicrobial experiment (i.e., the plate count assay). The results show a marginal decrease (~12%) in the bacterial count in the poly-L-lysine coated cloth compared to the control (Figure S6). Thus,

although the charge–charge interaction may play a role in the binding of *P. aeruginosa* to ZnO nanocrystals, the antimicrobial activity is predominantly due to the binding and subsequent denaturation of SARS-CoV-2 spike protein-mimicking protein of *P. aeruginosa*.

Next, we performed a computer simulation study to understand whether the filtration effect is due to the RBD mimic adsorbing to the ZnO crystals or due to some other blockade by the protrusions of the fibers and their new ZnO decoration. Particle (i.e., the microbe) flow through the cellulose fiber mesh was simulated using laminar flow and particle tracing algorithms as implemented in COMSOL multiphysics software. A simplified two-dimensional model of the cellulose fiber mesh (with ~10 μm pores) was built as depicted in Figure S7a, and the particle flow was studied through this mesh under normal exhalation conditions (*vide* Materials and Methods section for details of the parameters used; Figure S7b). ZnO deposition on the cellulose fiber slightly increased the diameters of such fibers (Figure 3a,b,e,f), which was ignored in the simulation. In this regard, it has to be noted that the sizes of the microbes are much smaller (~0.05–0.5 μm) compared to the pores. Particle penetration ability up to 100 μm of the cellulose fiber mesh was studied varying the sticking probability (i.e., the affinity) from 0.1 to 1 (per collision), and it was found that penetration ability decreases exponentially with the increase in sticking probability (Figure S7e). As evident from our microbial experiments, the sticking probability of the bare cotton cloth is very low (~10% or

~0.1). The simulation results show that with a sticking probability of 0.1, 20 layers of the fabric are required to trap ~98% of the particles. However, Figure 3 shows the alterations are of only 1−2 layers. On the contrary, molecular docking showed that binding free energy of SARS-CoV-2 RBD on the ⟨101⟩ facet of ZnO is −29 kcal/mol, indicating a very high binding affinity with a large equilibrium constant [1.82×10^{21} as obtained from $\Delta G = -R \times T \times \ln(k_{eq})$ equation]. Such a large k_{eq} suggests that almost all the particles remain bound and the sticking probability is close to 1. The simulation results demonstrate that even with a 90% sticking probability, all the particles got trapped within the first few layers of the cellulose fiber mesh (Figure S7e,f; Videos S1 and S2). Thus, the bare fibers or fiber protrusions alone cannot stop the spread of the microbe, while the ZnO-covered regions can instantly trap them due to their high binding affinity. Moreover, the bare fibers have not shown significant antimicrobial activity in our experiments. Therefore, the antimicrobial activity as depicted by the ZnO NF-fabricated cotton cloths is predominantly due to the attachment and subsequent denaturation of the spike-protein mimic by the ZnO surface.

Thus, our antimicrobial studies experimentally provide evidence that ZnO NF can induce membrane damage, resulting into a loss of membrane potential leading to inhibition of PI staining. It further depicts that ZnO NF is an effective antimicrobial agent particularly against SARS-CoV-2-mimicking microorganisms.

Washability and Reusability of the ZnO NF-Functionalized Cotton Fabric. For regular use as an antimicrobial hospital dress material (or PPE), washability and reusability of the fabric are the two major factors. To address this issue, we have washed the fabric material with a mild detergent as well as with a harsh detergent in tap water. Even after 50 washes with the mild detergent and 10 washes with the harsh detergent, the ZnO NF coating of the cotton fibers remained almost intact as observed under SEM (Figure S8). The antibacterial activity was also sustained in both the cases as compared to the original ZnO NF-functionalized fabric (Figure S9). Therefore, the ZnO NF-functionalized cotton fabric was found to be highly reusable with sufficient washability.

CONCLUSIONS

In conclusion, we successfully functionalized the commonly available cotton fabrics with ZnO NFs. The ZnO NF-functionalized cotton fabrics showed significant antimicrobial activities against the SARS-Cov-2 mimic model pathogenic microorganism as depicted in our detailed antimicrobial assays. The ZnO NFs were able to destroy the microbial membrane leading to inhibition of infection. A detailed computational study along with *in vitro* studies using viral spike protein-mimicking protein and bacteria showed the trapping ability of the fabric. As a proof of concept, we designed a laboratory-grade prototype respirator for using in common N95 masks using the ZnO NF-functionalized cotton fabrics. The porous respirator helped to solve the problem of CO_2 rebreathing and prevented spread of microbes through the pores. The ZnO NF-functionalized cotton fabrics can further be used to design comfortable, washable antimicrobial PPE, which is an urgent need of today.

MATERIALS AND METHODS

Synthesis of the ZnO NF-Functionalized Cotton Cloth (Patent Ref. No. 202031038152). Zinc nitrate hexahydrate [$Zn(NO_3)_2$, $6H_2O$; Sigma-Aldrich] and hexamethylenetetramine ($C_6H_{12}N_4$; Aldrich) were used as the starting materials for a low-temperature hydrothermal synthesis of ZnO NFs on the cotton fiber matrix.

For the synthesis of the ZnO-functionalized cotton cloth, at first, seed layer ZnO nanoparticles of ~5 nm in size were prepared in ethanol. In a typical synthesis process, to a 2 mM zinc acetate [$Zn(CH_3COO)_2 \cdot 2H_2O$; 20 mL in ethanol] solution heated at 55 °C, 4 mM sodium hydroxide (NaOH) solution (20 mL of ethanol) was dropwise added under continuous stirring conditions. The glass beaker was then covered tightly with aluminum foil and heated at 65 °C for 2 h with continuous stirring. After 2 h, the resultant transparent ZnO nanoparticle colloidal solution (seeding material) was allowed to cool down to room temperature and stored in a refrigerator for further use.

For seeding of the 5 nm ZnO particles on the cotton cloth, the cloths (3 cm × 3 cm) were dipped into the seeding solution for 10 min and then dried into a hot oven operating at 95 °C for 10 min. The procedure was repeated 11 times. Then, the cloth was transferred to an autoclave vessel. An aqueous solution of zinc nitrate (20 mM) and hexamethylenetetramine (20 mM) was used as the precursor solution for the ZnO NF growth, which was carried out at 102 °C for 15 h. This led to the growth of ZnO NFs with a length of ~600−850 nm and a diameter of ~150−300 nm. To maintain a constant growth rate of the ZnO NFs during the hydrothermal process, the old precursor solution was replaced with a fresh solution every 5 h. The as-obtained ZnO NF samples were then taken out of the reaction vessel and rinsed thoroughly with DI water to remove unreacted residues. Finally, the samples were annealed in air at ~110 °C for 3 h prior to the study.

Characterization Methods. Field emission SEM (QUANTA FEG 250) was used to investigate the surface morphology of the samples. TEM was carried out using an FEI (Technai S-Twin) instrument with an acceleration voltage of 200 kV. A drop of the sample (obtained by scratching the ZnO NF-decorated cotton cloth) was placed on a carbon-coated copper grid, and particle sizes were determined from micrographs recorded at a high magnification of 100,000×. XRD was used to characterize the crystal phase using a PANalytical X'Pert Pro diffractometer equipped with Cu Kα radiation (at 40 mA and 40 kV) at a scanning rate of 0.02° S^{-1} in the 2θ range from 20 to 80°. TG analysis (TGA) of PDPB, PDPB−ZnO, and ZnO solid powder was performed under a nitrogen atmosphere with a heating rate of 10 °C-min from 30 to 600 °C by using a PerkinElmer TGA-50H. For optical experiments, the steady-state absorption and emission were recorded with a JASCO V-750 spectrophotometer and a JASCO FP-8200 fluorimeter, respectively. Picosecond-resolved spectroscopic studies were carried out using a commercial time correlated single-photon counting setup from Edinburgh Instruments (instrument response function, IRF = 82 ps, excitation at 375 nm). The details of the experimental setup and methodology were described in our earlier report.[68] The average lifetime (amplitude-weighted) of a multiexponential decay is expressed as

$$\tau_{avg} = \sum_{i=1}^{N} c_i \tau_i$$

Computational Study. *Binding Study.* The optimized orthorhombic ZnO wurtzite unit cell (a = 5.63, b = 3.25, and c = 5.21) with eight atoms was taken to build a large supercell. For binding calculations on the ⟨002⟩, ⟨100⟩, and ⟨101⟩ facets, slabs of atoms with the exposed ⟨002⟩, ⟨100⟩, and ⟨101⟩ phases, respectively, were cut out of the bulk (supercell). For the calculation with a nanosphere, a sphere of a radius of 15 Å was cut out from the bulk and then appropriate surface atoms were removed to make it stoichiometrically neutral. The ACE2-bound SARS-CoV-2 spike protein structure (PDB ID: 6LZG) was obtained from the Protein Data Bank (PDB). ACE2 protein was removed before docking with the nanostructures. The structure of the lectin protein (PDB ID: 4YWA) of *P. aeruginosa* was also obtained from PDB. Molecular docking was performed using AutoDock Vina[39] following a previously published protocol.[40] The

docked structures were energy-minimized under OPLS using the Desmond molecular dynamics program[41] as implemented in Schrodinger Maestro (academic release 2018-4), followed by rescoring with AutoDock Vina. Changes in the atomic positions of the protein backbone after minimization were computed in terms of rmsd.

Sequence Analysis. The sequence of the cell surface adhesion lectin protein lecA of *P. aeruginosa* was obtained from the PDB (PDB ID: 4YWA). The structure and sequence of the RBD of SARS-CoV-2 were also obtained from the PDB (ID: 6LZG). Sequence alignment was performed using Clustal Omega[69] with no end gap penalty. Local alignments were performed with LALIGN.[70] Similar amino acids in the binding sites of the two proteins are mapped using PyMOL molecular graphics software.

Multiphysics Simulation. Particle (i.e., microbe) flow through the cotton mesh was simulated using laminar flow and particle tracing modules of COMSOL. A two-dimensional periodic model of the mesh was constructed as depicted in Figure S7a. The fiber diameter in the model is 10 μm, and the separation between fibers is also kept at 10 μm (*vide* Figure 3e−g). The velocity of exhaled air for laminar flow was 5.66 m s^{-1}. Considering the size of bacteria, viruses, and respiratory droplets (e.g., the SARS-CoV-2 diameter was 0.05−0.2 μm, the bacterium diameter was typically 0.5−5.0 μm; the respiratory droplet size during normal breathing was ∼1 μm), the particle size and density used were 1 μm and 1.1 g cm^3, respectively.[71] Particles move in the air velocity field (Figure S7b). On collision with a fiber, a particle either sticks to it or gets scattered. The probability of the particle sticking to the fibrils was set according to the binding energies with ZnO facets and cellulose fibrils. The simulation time was 0.1 s. The increase in the thickness of cellulose fibers due to ZnO deposition as seen in Figure 3a,b was ignored in the simulation.

Antibacterial Tests. The bacterial strains of Gram-negative *P. aeruginosa* and Gram-positive *S. aureus* as used in this study were obtained from Dey's Medical Stores Mfg. Ltd., Kolkata, India. The glassware, suction nozzles, and culture medium were sterilized in an autoclave at a high pressure of 0.1 MPa and a temperature of 120 °C for 30 min before experiments. Bacteria cultures were cultivated in a sterilized LB broth (Himedia, India), and incubation was done at 37 °C with a shaking incubator for 24 h.

The colony count method was used to estimate antibacterial properties through the concentration of the survival colony bacteria in co-cultured solution. First, original bacterial suspensions were washed three times with phosphate-buffered saline (PBS; pH 7.4) solution to a concentration of 10^8 CFU/mL. Then, they were poured onto the ZnO NF-functionalized cotton fabric and incubated for 1 h. Third, the incubated bacterial solution was diluted five times to a certain concentration. The resulting bacterial PBS suspensions (100 μL) were spread on gelatinous LB agar plates, culturing at 37 °C for 24 h. The number of survival colonies was counted manually. For growth curve analysis, the bacterial solution which was diluted five times was added to LB and kept at 37 °C. 600 nm absorbance (or optical density; OD$_{600}$) was monitored at regular intervals (1 h) to assess the growth kinetics.

The bacteria cells after proper incubation with the ZnO NF-functionalized cotton fabric were stained with DAPI and PI. The DAPI stains all cells, while PI only stains the membrane-disrupted cells. The $\left(1 - \frac{red}{blue}\right)$ ratio was obtained to assess the survivality of *P. aeruginosa*. Non-functionalized cotton cloths and untreated bacterial cultures were used as controls in all the tests. All tests were repeated at least six times.

To rule out the role of charge−charge interactions in the antimicrobial effect, we coated the cotton fabric with positively charged poly-L-lysine and performed the plate count experiment with *P. aeruginosa*, following the procedure described above.

Statistics. Data are represented as the mean ± standard deviation unless otherwise stated. One-way ANOVA, followed by Tukey's post hoc test, was used to calculate differences between groups. $P < 0.05$ was considered significant. For all statistical tests, GraphPad Prism (v8.0) software was used.

■ ASSOCIATED CONTENT

ⓢ Supporting Information

The Supporting Information is available free of charge at https://pubs.acs.org/doi/10.1021/acsabm.1c00238.

> Local alignment results between SARS-CoV-2 spike protein and lecA of *P. aeruginosa*; energy-dispersive X-ray analysis of the ZnO NF-decorated cotton cloth; elemental mapping showing the uniform distribution of ZnO NF over the cotton matrix; TG data of the ZnO NF-decorated cotton cloth and the bare cotton cloth; binding of ZnO with the cellulose fiber; antimicrobial activity of the ZnO NF-decorated cotton fabric on *S. aureus*, a Gram-negative bacterium; role of charge−charge interactions in the antimicrobial activity of the ZnO NF-decorated cotton fabric on *P. aeruginosa*; multiphysics simulation of particle tracing through the cellulose fiber mesh; role of washing with the detergent on the stability of the ZnO NF-functionalized cotton fabric; and role of washing with the detergent on the antimicrobial activity (*P. aeruginosa*) of the ZnO NF-functionalized cotton fabric (PDF)

> Multiphysics simulation of particle tracing through the cellulose fiber mesh (MPG)

> Multiphysics simulation of particle tracing through the ZnO NF functionalised cellulose fiber mesh (MPG)

■ AUTHOR INFORMATION

Corresponding Authors

Tanusri Saha-Dasgupta − *Technical Research Centre and Department of Condensed Matter Physics and Material Sciences, S. N. Bose National Centre for Basic Sciences, Kolkata 700106, India;* ⓞ orcid.org/0000-0001-6933-3151; Email: tanusri@bose.res.in

Samit Kumar Ray − *Department of Condensed Matter Physics and Material Sciences, S. N. Bose National Centre for Basic Sciences, Kolkata 700106, India; Department of Physics, Indian Institute of Technology Kharagpur, Kharagpur 721302, India;* Email: samit@bose.res.in

Samir Kumar Pal − *Department of Chemical, Biological and Macromolecular Sciences, S. N. Bose National Centre for Basic Sciences, Kolkata 700106, India; Technical Research Centre, S. N. Bose National Centre for Basic Sciences, Kolkata 700106, India;* ⓞ orcid.org/0000-0001-6943-5828; Email: skpal@bose.res.in

Authors

Aniruddha Adhikari − *Department of Chemical, Biological and Macromolecular Sciences, S. N. Bose National Centre for Basic Sciences, Kolkata 700106, India*

Uttam Pal − *Technical Research Centre, S. N. Bose National Centre for Basic Sciences, Kolkata 700106, India;* ⓞ orcid.org/0000-0003-2110-4610

Sayan Bayan − *Department of Condensed Matter Physics and Material Sciences, S. N. Bose National Centre for Basic Sciences, Kolkata 700106, India;* ⓞ orcid.org/0000-0002-7630-8146

Susmita Mondal − *Department of Chemical, Biological and Macromolecular Sciences, S. N. Bose National Centre for Basic Sciences, Kolkata 700106, India*

Ria Ghosh − *Technical Research Centre, S. N. Bose National Centre for Basic Sciences, Kolkata 700106, India*

Soumendra Darbar − *Research & Development Division, Dey's Medical Stores (Mfg.) Ltd., Kolkata 700019, India*

Complete contact information is available at:
https://pubs.acs.org/10.1021/acsabm.1c00238

Author Contributions

A.A., S.B., S.M., and R.G. performed the experiments. U.P. did the *in silico* studies. A.A., U.P., S.B., S.D., T.S.-D., S.K.R., and S.K.P. planned the study and analyzed the results. A.A. wrote the initial draft of the manuscript. A.A. made all the illustrations including the graphical abstract. All authors have corrected and modified the manuscript and approved for submission.

Notes

The authors declare no competing financial interest.

■ REFERENCES

(1) Deming, M. E.; Michael, N. L.; Robb, M.; Cohen, M. S.; Neuzil, K. M. Accelerating Development of SARS-CoV-2 Vaccines — The Role for Controlled Human Infection Models. *N. Engl. J. Med.* **2020**, *383*, No. e63.

(2) Johns Hopkins University. COVID-19 Dashboard by the Center for Systems Science and Engineering (CSSE) at Johns Hopkins University (JHU). https://coronavirus.jhu.edu/map.html (accessed Dec 29, 2020).

(3) Talebian, S.; Wallace, G. G.; Schroeder, A.; Stellacci, F.; Conde, J. Nanotechnology-based disinfectants and sensors for SARS-CoV-2. *Nat. Nanotechnol.* **2020**, *15*, 618−621.

(4) Haushofer, J.; Metcalf, C. J. E. Which interventions work best in a pandemic? *Science* **2020**, *368*, 1063−1065.

(5) Ma, Q. X.; Shan, H.; Zhang, H. L.; Li, G. M.; Yang, R. M.; Chen, J. M. Potential utilities of mask-wearing and instant hand hygiene for fighting SARS-CoV-2. *J. Med. Virol.* **2020**, *92*, 1567−1571.

(6) Leung, N. H. L.; Chu, D. K. W.; Shiu, E. Y. C.; Chan, K.-H.; McDevitt, J. J.; Hau, B. J. P.; Yen, H.-L.; Li, Y.; Ip, D. K. M.; Peiris, J. S. M.; Seto, W.-H.; Leung, G. M.; Milton, D. K.; Cowling, B. J. Respiratory virus shedding in exhaled breath and efficacy of face masks. *Nat. Med.* **2020**, *26*, 676−680.

(7) Fischer, E. P.; Fischer, M. C.; Grass, D.; Henrion, I.; Warren, W. S.; Westman, E. Low-cost measurement of face mask efficacy for filtering expelled droplets during speech. *Sci. Adv.* **2020**, *6*, No. eabd3083.

(8) Centers for Disease Control and Prevention (CDC). Considerations for Wearing Masks. https://www.cdc.gov/coronavirus/2019-ncov/prevent-getting-sick/cloth-face-cover-guidance.html (accessed August 30, 2020).

(9) Morishima, M.; Mitsuno, T.; Kishida, K. Problems related to mask use in hay fever sufferers by repeated surveys. *Inter. J. Cloth. Sci. Tech.* **2017**, *29*, 123−134.

(10) Lee, H. P.; de Wang, Y. Objective Assessment of Increase in Breathing Resistance of N95 Respirators on Human Subjects. *Ann. Occup. Hyg.* **2011**, *55*, 917−921.

(11) Roberge, R. J.; Coca, A.; Williams, W. J.; Powell, J. B.; Palmiero, A. J. Physiological Impact of the N95 Filtering Facepiece Respirator on Healthcare Workers. *Respir. Care* **2010**, *55*, 569−577.

(12) Kyung, S. Y.; Kim, Y.; Hwang, H.; Park, J.-W.; Jeong, S. H. Risks of N95 Face Mask Use in Subjects With COPD. *Respir. Care* **2020**, *65*, 658−664.

(13) Li, Y.; Tokura, H.; Guo, Y. P.; Wong, A. S. W.; Wong, T.; Chung, J.; Newton, E. Effects of wearing N95 and surgical facemasks on heart rate, thermal stress and subjective sensations. *Int. Arch. Occup. Environ. Health* **2005**, *78*, 501−509.

(14) Rodríguez-Tobías, H.; Morales, G.; Grande, D. Comprehensive review on electrospinning techniques as versatile approaches toward antimicrobial biopolymeric composite fibers. *Mater. Sci. Eng., C* **2019**, *101*, 306−322.

(15) Salmond, G. P.; Welch, M. Antibiotic resistance: adaptive evolution. *Lancet* **2008**, *372*, S97−S103.

(16) Spellberg, B.; Bartlett, J. G.; Gilbert, D. N. The Future of Antibiotics and Resistance. *N. Engl. J. Med.* **2013**, *368*, 299−302.

(17) Xiu, Z.-m.; Zhang, Q.-b.; Puppala, H. L.; Colvin, V. L.; Alvarez, P. J. J. Negligible Particle-Specific Antibacterial Activity of Silver Nanoparticles. *Nano Lett.* **2012**, *12*, 4271−4275.

(18) Shrivastava, S.; Bera, T.; Roy, A.; Singh, G.; Ramachandrarao, P.; Dash, D. Characterization of enhanced antibacterial effects of novel silver nanoparticles. *Nanotechnology* **2007**, *18*, 225103.

(19) Shi, Z.; Tang, J.; Chen, L.; Yan, C.; Tanvir, S.; Anderson, W. A.; Berry, R. M.; Tam, K. C. Enhanced colloidal stability and antibacterial performance of silver nanoparticles/cellulose nanocrystal hybrids. *J. Mater. Chem. B* **2015**, *3*, 603−611.

(20) MubarakAli, D.; Thajuddin, N.; Jeganathan, K.; Gunasekaran, M. Plant extract mediated synthesis of silver and gold nanoparticles and its antibacterial activity against clinically isolated pathogens. *Colloids Surf. B Biointerfaces* **2011**, *85*, 360−365.

(21) Zhao, Y.; Tian, Y.; Cui, Y.; Liu, W.; Ma, W.; Jiang, X. Small Molecule-Capped Gold Nanoparticles as Potent Antibacterial Agents That Target Gram-Negative Bacteria. *J. Am. Chem. Soc.* **2010**, *132*, 12349−12356.

(22) Zhao, Y.; Ye, C.; Liu, W.; Chen, R.; Jiang, X. Tuning the Composition of AuPt Bimetallic Nanoparticles for Antibacterial Application. *Angew. Chem., Int. Ed.* **2014**, *53*, 8127−8131.

(23) Gopinath, K.; Kumaraguru, S.; Bhakyaraj, K.; Mohan, S.; Venkatesh, K. S.; Esakkirajan, M.; Kaleeswarran, P.; Alharbi, N. S.; Kadaikunnan, S.; Govindarajan, M.; Benelli, G.; Arumugam, A. Green synthesis of silver, gold and silver/gold bimetallic nanoparticles using the Gloriosa superba leaf extract and their antibacterial and antibiofilm activities. *Microb. Pathog.* **2016**, *101*, 1−11.

(24) Szunerits, S.; Boukherroub, R. Antibacterial activity of graphene-based materials. *J. Mater. Chem. B* **2016**, *4*, 6892−6912.

(25) Marciano, F. R.; Lima-Oliveira, D. A.; Da-Silva, N. S.; Diniz, A. V.; Corat, E. J.; Trava-Airoldi, V. J. Antibacterial activity of DLC films containing TiO2 nanoparticles. *J. Colloid Interface Sci.* **2009**, *340*, 87−92.

(26) Li, Y.; Zhang, W.; Niu, J.; Chen, Y. Mechanism of Photogenerated Reactive Oxygen Species and Correlation with the Antibacterial Properties of Engineered Metal-Oxide Nanoparticles. *ACS Nano* **2012**, *6*, 5164−5173.

(27) Alvarez, G. S.; Hélary, C.; Mebert, A. M.; Wang, X.; Coradin, T.; Desimone, M. F. Antibiotic-loaded silica nanoparticle−collagen composite hydrogels with prolonged antimicrobial activity for wound infection prevention. *J. Mater. Chem. B* **2014**, *2*, 4660−4670.

(28) Kim, Y. S.; Song, M. Y.; Park, J. D.; Song, K. S.; Ryu, H. R.; Chung, Y. H.; Chang, H. K.; Lee, J. H.; Oh, K. H.; Kelman, B. J.; Hwang, I. K.; Yu, I. J. Subchronic oral toxicity of silver nanoparticles. *Part. Fibre Toxicol.* **2010**, *7*, 20.

(29) Beer, C.; Foldbjerg, R.; Hayashi, Y.; Sutherland, D. S.; Autrup, H. Toxicity of silver nanoparticles—Nanoparticle or silver ion? *Toxicol. Lett.* **2012**, *208*, 286−292.

(30) Kittler, S.; Greulich, C.; Diendorf, J.; Küller, M.; Epple, M. Toxicity of Silver Nanoparticles Increases during Storage Because of Slow Dissolution under Release of Silver Ions. *Chem. Mater.* **2010**, *22*, 4548−4554.

(31) Jeng, H. A.; Swanson, J. Toxicity of Metal Oxide Nanoparticles in Mammalian Cells. *J. Environ. Sci. Health, Part A: Toxic/Hazard. Subst. Environ. Eng.* **2006**, *41*, 2699−2711.

(32) Djurišić, A. B.; Leung, Y. H.; Ng, A. M. C.; Xu, X. Y.; Lee, P. K. H.; Degger, N.; Wu, R. S. S. Toxicity of Metal Oxide Nanoparticles:

Mechanisms, Characterization, and Avoiding Experimental Artefacts. *Small* **2015**, *11*, 26−44.

(33) Zheng, K.; Setyawati, M. I.; Leong, D. T.; Xie, J. Antimicrobial Gold Nanoclusters. *ACS Nano* **2017**, *11*, 6904−6910.

(34) Haidari, H.; Kopecki, Z.; Bright, R.; Cowin, A. J.; Garg, S.; Goswami, N.; Vasilev, K. Ultrasmall AgNP-Impregnated Biocompatible Hydrogel with Highly Effective Biofilm Elimination Properties. *ACS Appl. Mater. Interfaces* **2020**, *12*, 41011−41025.

(35) Zheng, K.; Setyawati, M. I.; Leong, D. T.; Xie, J. Observing antimicrobial process with traceable gold nanoclusters. *Nano Res.* **2021**, *14*, 1026−1033.

(36) Zheng, K.; Xie, J. Composition-Dependent Antimicrobial Ability of Full-Spectrum AuxAg25−x Alloy Nanoclusters. *ACS Nano* **2020**, *14*, 11533−11541.

(37) Zheng, K.; Xie, J. Engineering Ultrasmall Metal Nanoclusters as Promising Theranostic Agents. *Trends Chem.* **2020**, *2*, 665−679.

(38) Bian, J.; Li, Z. Angiotensin-converting enzyme 2 (ACE2): SARS-CoV-2 receptor and RAS modulator. *Acta Pharm. Sin. B* **2021**, *11*, 1.

(39) Bourgonje, A. R.; Abdulle, A. E.; Timens, W.; Hillebrands, J. L.; Navis, G. J.; Gordijn, S. J.; Bolling, M. C.; Dijkstra, G.; Voors, A. A.; Osterhaus, A. D.; Voort, P. H.; Mulder, D. J.; Goor, H. Angiotensin-converting enzyme 2 (ACE2), SARS-CoV-2 and the pathophysiology of coronavirus disease 2019 (COVID-19). *J. Pathol.* **2020**, *251*, 228−248.

(40) Li, W.; Moore, M. J.; Vasilieva, N.; Sui, J.; Wong, S. K.; Berne, M. A.; Somasundaran, M.; Sullivan, J. L.; Luzuriaga, K.; Greenough, T. C.; Choe, H.; Farzan, M. Angiotensin-converting enzyme 2 is a functional receptor for the SARS coronavirus. *Nature* **2003**, *426*, 450−454.

(41) Kirchdoerfer, R. N.; Cottrell, C. A.; Wang, N.; Pallesen, J.; Yassine, H. M.; Turner, H. L.; Corbett, K. S.; Graham, B. S.; McLellan, J. S.; Ward, A. B. Pre-fusion structure of a human coronavirus spike protein. *Nature* **2016**, *531*, 118−121.

(42) Hoffmann, M.; Kleine-Weber, H.; Schroeder, S.; Krüger, N.; Herrler, T.; Erichsen, S.; Schiergens, T. S.; Herrler, G.; Wu, N.-H.; Nitsche, A.; Müller, M. A.; Drosten, C.; Pöhlmann, S. SARS-CoV-2 Cell Entry Depends on ACE2 and TMPRSS2 and Is Blocked by a Clinically Proven Protease Inhibitor. *Cell* **2020**, *181*, 271−280.

(43) Biswas, P.; Adhikari, A.; Pal, U.; Singh, P.; Das, M.; Saha-Dasgupta, T.; Choudhury, S. S.; Das, R.; Pal, S. K. Flexibility modulates the catalytic activity of a thermostable enzyme: key information from optical spectroscopy and molecular dynamics simulation. *Soft Matter* **2020**, *16*, 3050−3062.

(44) Dutta, R. K.; Nenavathu, B. P.; Gangishetty, M. K.; Reddy, A. V. R. Studies on antibacterial activity of ZnO nanoparticles by ROS induced lipid peroxidation. *Colloids Surf. B Biointerfaces* **2012**, *94*, 143−150.

(45) Tavakoli, A.; Ataei-Pirkooh, A.; Sadeghi, G. M M.; Bokharaei-Salim, F.; Sahrapour, P.; Kiani, S. J.; Moghoofei, M.; Farahmand, M.; Javanmard, D.; Monavari, S. H. Polyethylene glycol-coated zinc oxide nanoparticle: an efficient nanoweapon to fight against herpes simplex virus type 1. *Nanomedicine* **2018**, *13*, 2675−2690.

(46) Li, Z.; Yang, R.; Yu, M.; Bai, F.; Li, C.; Wang, Z. L. Cellular Level Biocompatibility and Biosafety of ZnO Nanowires. *J. Phys. Chem. C* **2008**, *112*, 20114−20117.

(47) Madathiparambil Visalakshan, R.; González García, L. E.; Benzigar, M. R.; Ghazaryan, A.; Simon, J.; Mierczynska-Vasilev, A.; Michl, T. D.; Vinu, A.; Mailänder, V.; Morsbach, S.; Landfester, K.; Vasilev, K. The Influence of Nanoparticle Shape on Protein Corona Formation. *Small* **2020**, *16*, 2000285.

(48) Roach, P.; Farrar, D.; Perry, C. C. Surface Tailoring for Controlled Protein Adsorption: Effect of Topography at the Nanometer Scale and Chemistry. *J. Am. Chem. Soc.* **2006**, *128*, 3939−3945.

(49) Chemani, C.; Imberty, A.; de Bentzmann, S.; Pierre, M.; Wimmerová, M.; Guery, B. P.; Faure, K. Role of LecA and LecB Lectins in Pseudomonas aeruginosa-Induced Lung Injury and Effect of Carbohydrate Ligands. *Infect. Immun.* **2009**, *77*, 2065−2075.

(50) Lyczak, J. B.; Cannon, C. L.; Pier, G. B. Lung Infections Associated with Cystic Fibrosis. *Clin. Microbiol. Rev.* **2002**, *15*, 194−222.

(51) Fagon, J.-Y.; Chastre, J.; Domart, Y.; Trouillet, J.-L.; Gibert, C. Mortality Due to Ventilator-Associated Pneumonia or Colonization with Pseudomonas or Acinetobacter Species: Assessment by Quantitative Culture of Samples Obtained by a Protected Specimen Brush. *Clin. Infect. Dis.* **1996**, *23*, 538−542.

(52) Weng, B.; Yang, M.-Q.; Zhang, N.; Xu, Y.-J. Toward the enhanced photoactivity and photostability of ZnO nanospheres via intimate surface coating with reduced graphene oxide. *J. Mater. Chem. A* **2014**, *2*, 9380−9389.

(53) Mamat, M. H.; Khusaimi, Z.; Zahidi, M. M.; Bakar, S. A.; Siran, Y. M.; Rejab, S. A. M.; Asis, A. J.; Tahiruddin, S.; Abdullah, S.; Mahmood, M. R. Controllable Growth of Vertically Aligned Aluminum-Doped Zinc Oxide Nanorod Arrays by Sonicated Sol−Gel Immersion Method depending on Precursor Solution Volumes. *Jpn. J. Appl. Phys.* **2011**, *50*, 06GH04.

(54) Sathe, P.; Laxman, K.; Myint, M. T. Z.; Dobretsov, S.; Richter, J.; Dutta, J. Bioinspired nanocoatings for biofouling prevention by photocatalytic redox reactions. *Sci. Rep.* **2017**, *7*, 3624.

(55) Seddigi, Z. S.; Ahmed, S. A.; Sardar, S.; Pal, S. K. Ultrafast dynamics at the zinc phthalocyanine/zinc oxide nanohybrid interface for efficient solar light harvesting in the near red region. *Sol. Energy Mater. Sol. Cells* **2015**, *143*, 63−71.

(56) Bayan, S.; Mohanta, D. Directed growth characteristics and optoelectronic properties of Eu-doped ZnO nanorods and urchins. *J. Appl. Phys.* **2010**, *108*, 023512.

(57) Zhang, H.; Yang, D.; Ji, Y.; Ma, X.; Xu, J.; Que, D. Low Temperature Synthesis of Flowerlike ZnO Nanostructures by Cetyltrimethylammonium Bromide-Assisted Hydrothermal Process. *J. Phys. Chem. B* **2004**, *108*, 3955−3958.

(58) Castellan, A.; Ruggiero, R.; Frollini, E.; Ramos, L. A.; Chirat, C. Studies on fluorescence of cellulosics. *Holzforschung* **2007**, *61*, 504.

(59) Vinod, R.; Sajan, P.; Achary, S. R.; Tomas, C. M.; Muñoz-Sanjosé, V.; Bushiri, M. J. Enhanced UV emission from ZnO nanoflowers synthesized by the hydrothermal process. *J. Phys. D: Appl. Phys.* **2012**, *45*, 425103.

(60) Yang, W.; Li, Q.; Gao, S.; Shang, K. J. NH4+ directed assembly of zinc oxide micro-tubes from nanoflakes. *Nanoscale Res. Lett.* **2011**, *6*, 491.

(61) Grönroos, P.; Bessonoff, M.; Salminen, K.; Paltakari, J.; Kulmala, S. Phosphorescence and fluorescence of fibrillar cellulose films. *Nord. Pulp Pap. Res. J.* **2018**, *33*, 246.

(62) Gavrilov, M. Z.; Ermolenko, I. N. A study of cellulose luminescence. *J. Appl. Spectrosc.* **1966**, *5*, 542−544.

(63) Kitaoka, T.; Isogai, A.; Onabe, F. Chemical modification of pulp fibers by TEMPO-mediated oxidation. *Nord. Pulp Pap. Res. J.* **1999**, *14*, 279.

(64) Ma, H.; Ma, W.; Chen, J.-F.; Liu, X.-Y.; Peng, Y.-Y.; Yang, Z.-Y.; Tian, H.; Long, Y.-T. Quantifying Visible-Light-Induced Electron Transfer Properties of Single Dye-Sensitized ZnO Entity for Water Splitting. *J. Am. Chem. Soc.* **2018**, *140*, 5272−5279.

(65) Eschbach, M.; Schreiber, K.; Trunk, K.; Buer, J.; Jahn, D.; Schobert, M. Long-Term Anaerobic Survival of the Opportunistic Pathogen Pseudomonas aeruginosa via Pyruvate Fermentation. *J. Bacteriol.* **2004**, *186*, 4596.

(66) Kora, A. J.; Arunachalam, J. Assessment of antibacterial activity of silver nanoparticles on Pseudomonas aeruginosa and its mechanism of action. *World J. Microbiol. Biotechnol.* **2011**, *27*, 1209−1216.

(67) Halbus, A. F.; Horozov, T. S.; Paunov, V. N. Surface-Modified Zinc Oxide Nanoparticles for Antialgal and Antiyeast Applications. *ACS Appl. Nano Mater.* **2020**, *3*, 440−451.

(68) Bora, T.; Lakshman, K. K.; Sarkar, S.; Makhal, A.; Sardar, S.; Pal, S. K.; Dutta, J. Modulation of defect-mediated energy transfer from ZnO nanoparticles for the photocatalytic degradation of bilirubin. *Beilstein J. Nanotechnol.* **2013**, *4*, 714−725.

(69) Sievers, F.; Wilm, A.; Dineen, D.; Gibson, T. J.; Karplus, K.; Li, W.; Lopez, R.; McWilliam, H.; Remmert, M.; Söding, J.; Thompson, J.

D.; Higgins, D. G. Fast, scalable generation of high-quality protein multiple sequence alignments using Clustal Omega. *Mol. Syst. Biol.* **2011**, *7*, 539.

(70) Huang, X.; Miller, W. A time-efficient, linear-space local similarity algorithm. *Adv. Appl. Math.* **1991**, *12*, 337−357.

(71) Loferer-Krößbacher, M.; Klima, J.; Psenner, R. Determination of Bacterial Cell Dry Mass by Transmission Electron Microscopy and Densitometric Image Analysis. *Appl. Environ. Microbiol.* **1998**, *64*, 688.